Vibrational Spectroscopic Characterization of Hematite, Maghemite, and Magnetite Thin Films Produced by Vapor Deposition

Aaron M. Jubb and Heather C. Allen*

Department of Chemistry, The Ohio State University, 100 West 18th Avenue, Columbus, Ohio 43210

ABSTRACT Thin films of three iron oxide polymorphs, hematite, maghemite, and magnetite, were produced on KBr substrates using a conventional electron beam deposition technique coupled with thermal annealing. This method allowed for iron oxide thin films free from chemical precursor contaminants. The films were characterized using Fourier-transform infrared spectroscopy (FTIR), Raman microspectroscopy, and ellipsometry. These spectroscopic techniques allowed for a clear assignment of the phase of the iron oxide polymorph films produced along with an examination of the degree of crystallinity possessed by the films. The films produced were uniform in phase and exhibited decreasing crystallinity as the thickness increased from 40 to 250 nm.

KEYWORDS: Raman microspectroscopy • Fourier transform infrared spectroscopy • hematite • maghemite • magnetite • vapor deposition

INTRODUCTION

Iron oxides constitute an important class of materials that are ubiquitous in nature. There are 16 various iron oxide-oxyhydroxide polymorphs that display a wide range of properties and behavior in the environment (1). Because of this assortment of physical properties, iron oxides are of great interest to a variety of scientific disciplines for various applications that range from opto-electronics, medicine, environmental remediation, pigments, corrosion protection, and gas sensing, among others (1). Three of the most common and important iron oxide polymorphs are hematite (α-Fe$_2$O$_3$), maghemite (γ-Fe$_2$O$_3$), and magnetite (Fe$_3$O$_4$).

Hematite is the most common iron oxide polymorph found in nature because of its high thermodynamic stability. It is isostructural with corundum (α-Al$_2$O$_3$) having a hexagonal unit cell based on anion hcp packing (1). Because of its ubiquity in nature, the adsorptive properties of hematite are of great importance for the study of transport of contaminants in water and the remediation of waste (2−7). Maghemite, similar to hematite, is a fully oxidized iron oxide polymorph where all iron is in the Fe^{3+} state (1). The maghemite crystal structure possesses 2 and 1/3 vacant sites within its unit cell (1). If these vacant sites are randomly distributed within the crystal structure, then maghemite possesses an inverse spinel structure, similar to magnetite (8−10). The inverse spinel crystal structure is the most general case for maghemite (8, 9). It is an important intermediate to hematite formation from the oxidation of magnetite or the dehydroxylation of goethite precursors (1). Magnetite is a ferromagnetic material that is of importance to the electro-optical industry.

Found in nature, magnetite produces the magnetic behavior of rocks. Magnetite has an inverse spinel crystal structure, as mentioned above, where each unit cell consists of 8 Fe^{2+}, 16 Fe^{3+}, and 32 O^{2-} atoms (1, 11). It is an important precursor to hematite via thermal transformation processes.

$$Fe_3O_4 \xrightarrow{\geq 200\ °C} \gamma\text{-}Fe_2O_3 \xrightarrow{\geq 400\ °C} \alpha\text{-}Fe_2O_3 \qquad (1)$$
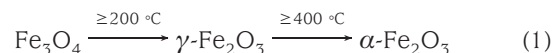
Synthetic thin films of the various iron oxide-oxyhydroxide polymorphs have been widely reported in the literature (12−41). General preparation approaches range from ultra-high vacuum epitaxial methods (26−29, 31−40) first reported in 1988 by Vuren et al. (26) involving the synthesis of single monolayers of iron oxides upon an oriented single-crystal substrate, generally Pt(111), to high vacuum methods such as chemical (16, 23) and physical vapor (12, 13, 21, 30) deposition to nonvacuum methods such as forced hydrolysis and sol−gel synthesis (14, 15, 19, 22). Although the use of ultrahigh vacuum epitaxial techniques produce very clean, well-defined, single-crystal films of iron oxide, the low-pressure requirement limits this method. Wet deposition and chemical vapor deposition techniques have also been shown to produce well-defined iron oxide films; however, the use of chemical precursors in these methods can leave contaminants (NO$_3^-$, SO$_4^{2-}$, organics) absorbed onto the thin film of interest. This is a major weakness of these methods if the thin films produced are to be used in adsorption studies. One of the earliest reported techniques for generating thin films is PVD by conventional electron-beam evaporation of an elemental metal either onto a hot substrate or followed by an annealing step in air (41). This technique seems to be less favored than other iron oxide production schemes as it requires both a high vacuum system, is a two step process, and generally produces polycrystalline films.

However, with the use of conventional electron-beam evaporation and a careful choice of annealing temperature (eq 1), it is possible to produce magnetite, maghemite, and hematite films without the presence of chemical precursors.

Raman and Fourier transform infrared (FTIR) spectroscopies have been used to characterize iron oxides for several decades (42−55). These analytical techniques can provide clear assignment of the oxide phase as well as a measurement of the degree of crystallinity of the materials under study through the observation of the phonon modes. Raman and IR spectroscopies are also ideal to study films too thin (<100 nm) to be studied easily by more conventional crystal characterization techniques, e.g., X-ray diffraction (XRD). Raman spectroscopy is generally the vibrational spectroscopy of choice when characterizing oxide powders and films as the various iron oxide polymorphs exhibit distinct Raman signatures and it is possible to take advantage of so-called phonon confinement effects to better quantify the crystallinity of the sample (10, 44, 45, 47, 49, 50, 54, 56−65). FTIR has been used less frequently to characterize iron oxide thin films, but can provide additional confirmation of the oxide phase present as well as information on the crystallinity of the film (16, 19, 50).

In this study, we present the preparation of polycrystalline thin (40−250 nm) hematite, maghemite, and magnetite films through the use of conventional electron-beam evaporation. These films are primarily characterized with Raman microspectroscopy with FTIR providing additional information on the phase of the films excluding the thicker magnetite film. This characterization allows for phase identification as well as insight into the degree of film crystallinity and uniformity.

EXPERIMENTAL SECTION

Materials. Iron oxide films were prepared by depositing a set amount of elemental iron onto KBr substrates via a conventional PVD technique, electron-beam evaporation using a thermal evaporator (Denton, model DV-502A). Here iron films of 20 and 100 nm were deposited via electron beam evaporation from elemental iron slugs (Alfa Aesar, 1/4 in. diameter by 1/4 in. length, 99.95 % pure) onto KBr substrates in a vacuum chamber at 4×10^{-6} Torr. The KBr discs measured 25 mm in diameter by 3 mm thick (Pike Technologies Inc.) and were used as received. Iron film thickness was controlled through the use of a quartz microbalance within the evaporation chamber. To produce iron oxide phases of interest, we annealed the iron films in a conventional muffle furnace (Fisher Scientific, Isotemp model 550−14) for 4 h in an air atmosphere (47, 66). To produce magnetite films, we annealed the deposited iron films in air at 175 °C, for maghemite, 350 °C in air, and for hematite, 575 °C in air. The annealing temperatures chosen resulted in films that were homogeneous in the desired iron oxide phase. Postannealing, the films were characterized with Raman microspectroscopy, FTIR, and ellipsometry.

Characterization. All Raman spectra were collected using a Renshaw inVia Raman microscope with a 50x objective coupled to a 632.8 nm He−Ne laser excitation source (Renshaw RL633). The resolution of this instrument was approximately 3 cm^{-1} with an 1800 groove/mm grating. Utilizing this setup the laser power at the sample was approximately 6 mWatts with 100 % laser power. Several studies (47, 57) have shown that iron oxides are vulnerable to heat-induced phase changes via the

Table 1. Iron Oxide Phases Produced and Thicknesses

oxide phase	Fe deposited (nm)	estimated thickness of oxide (nm)	ellipsometric measured thickness of oxide (nm)
hematite	20	49	47.2
	100	247	240.4
maghemite	20	46	48.0
	100	231	228.4
magnetite	20	42	41.2
	100	209	194.5

excitation source during the course of collecting a Raman spectrum. To address this issue, we utilized a line focus that produces a line shape for the excitation source at the sample surface that is approximately 5×40 μm in dimension. This effectively reduces the energy flux felt by any local spot on the sample surface preventing any phase changes in the iron oxide films during the course of a spectral acquisition. The Raman spectra presented in this study were collected with a 30 s acquisition time and 6 mW (100 %) laser power over a spectral range from 100−2000 cm^{-1}. However, as all diagnostic phonon modes for the iron oxide phases of interest occur below 1000 cm^{-1}, all Raman spectra are only presented from 100−1000 cm^{-1}. Raman spectra with the full 100−2000 cm^{-1} range can be found in the Supporting Information. Using these parameters, no phase changes were observed in the Raman spectra during the course of the spectral collection. FTIR spectra were collected in a Perkin-Elmer Spectrum 100 FTIR spectrometer equipped with a deuterated triglycine sulfate (DTGS) detector. The resolution used was 4 cm^{-1}. All spectra were collected with 400 scans in transmission mode, then referenced against a 3 mm blank KBr transmission spectrum to yield the absorbance spectra presented. No comparison between films of differing iron oxide phases is reported because of differing film thickness between the iron oxide films produced in this study. The FTIR spectrum of the thicker magnetite film is not reported because of excessive reflection losses from the film's mirror like surface.

Film thickness was calculated (Appendix A) and measured using ellipsometry with values reported in Table 1. Ellipsometry measurements were taken with a Gaertner L116s ellipsometer (Nanotech West Facility, Ohio State University) equipped with a 632.8 nm He−Ne laser. The ellipsometry measurements were carried out with an incident/collection angle of 70° using the thin oxide setting in the software program GEMP. In this setting, it is necessary to provide the software an initial estimate of the oxide film's refractive index and thickness. Here, bulk values of the refractive index for the iron oxides at 633 nm were provided and the thickness estimate was based upon the calculated estimate of the thickness using a unit-cell approach. Thickness characterization was carried out post-phase characterization in order to prevent laser-induced phase changes during ellipsometry measurements. The estimated and measured thickness, Table 1, agree within ±15 nm.

RESULTS AND DISCUSSION

Hematite. Hematite's irreducible vibrational modes at the first Brillouin zone center are represented by eq 2:

$$\Gamma_{vib} = 2A_{1g} + 2A_{1u} + 3A_{2g} + 2A_{2u} + 5E_{g} + 4E_{u}$$

(2)

The acoustic A_{1u} and the A_{2u} modes are optically silent, the symmetrical modes are Raman active, and the antisymmet-
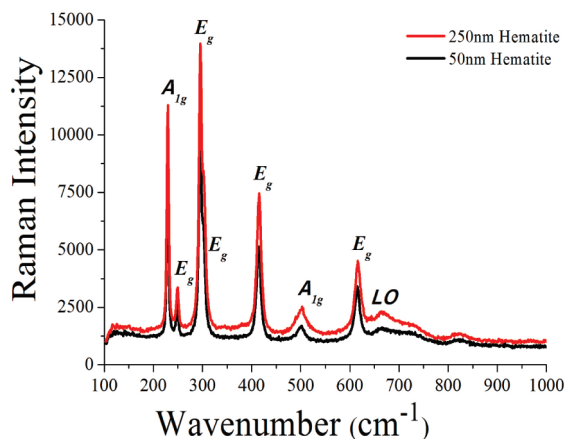
FIGURE 1. Raman spectra of hematite films. The seven peaks characteristic of hematite are present with no magnetite or maghemite contaminant peaks observed. LO Eu peak at 660 cm^{-1} indicated.

Table 2.   Observed Raman Active Phonon Modes for Iron Oxide Phases[a]

oxide	Raman shift (cm^{-1}) and assignment
hematite	229 (A_{1g}), 249 (E_g), 295 (E_g), 302 (E_g), 414 (E_g), 500 (A_{1g}), 615 (E_g), 660 (LO E_u)
maghemite	365 (T_{2g}), 511 (E_g), 700 (A_{1g})
magnetite	310 (T_{2g}), 554 (T_{2g}), 672 (A_{1g})

[a] Frequency of the Raman shifts are from this study, assignments from (10, 15, 49).

ric modes are infrared active (43, 50). As the hexagonal crystal structure of hematite features an inversion center, no modes are both Raman and infrared active (67). Figure 1 shows the Raman spectra of the iron oxide films produced after heating 20 and 100 nm Fe films at 575° for four hours in an air atmosphere. These spectra exhibit all seven of the spectral signatures deemed diagnostic for hematite, Table 2 (10, 47, 48, 50, 57), and do not contain any peaks associated with either maghemite or magnetite. The peaks seen at 229 cm^{-1} and 500 cm^{-1} are assigned to the A_{1g} modes (10). The remaining five peaks at 249, 295, 302, 414, and 615 cm^{-1} are assigned to the E_g modes (10). This indicates that heating for 4 h at 575 °C is suitable for transforming the initial Fe films completely to hematite. The weak peak seen at approximately 660 cm^{-1} has been widely observed in Raman spectra of hematite and is generally attributed to the presence of residual magnetite or maghemite contamination (47, 51−53, 57). However, the presence of magnetite or maghemite in the hematite films seems counterintuitive as the films were heated well above the temperature at which magnetite and maghemite are known to undergo complete thermal transformation to hematite in the presence of air (1). This issue has been noted by several other authors (15, 50, 54, 68), who have also observed the 660 cm^{-1} peak for hematite samples at elevated temperatures. Bersani et al. (15) showed that only by mixing hematite and magnetite powders together in a 1:1 ratio were they able to achieve the relative intensity for the 660 cm^{-1} peak that they had observed in their hematite film sample. This leads to the rejection of a residual magnetite presence
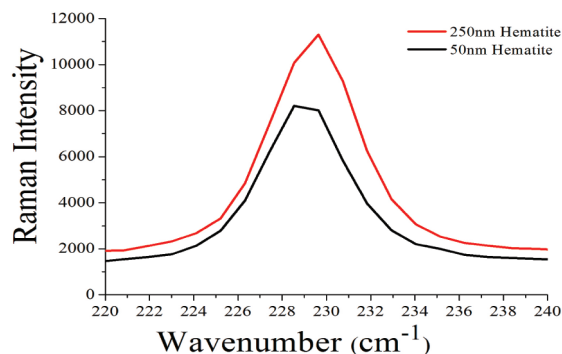

FIGURE 2. Raman spectra of A_{1g} peak at 229 cm^{-1} for both hematite films showing blue shift and broadening of the phonon mode for the 250 nm film relative to the 50 nm film.

as the source of the 660 cm^{-1} peak and the assignment of the 660 cm^{-1} peak to the Raman forbidden, IR active longitudinal optical (LO) E_u mode of hematite that occurs at the same frequency. This mode is thought to be activated by disorder within the hematite crystal lattice (15). This assignment was subsequently confirmed by others (50, 54, 68) and is adopted for this study.

Beyond phase assignment via observation of characteristic phonon peaks for oxide samples, Raman spectroscopy has been utilized extensively to investigate the crystallinity of micro- and nanoregimes through phonon confinement effects (54, 56, 58−62, 64, 65). Briefly, phonon confinement effects describe the phenomena that occurs with the lifting of the phonon momentum selection rule $q \approx 0$, for the Raman scattering process within ordered media. This generally occurs as crystal domains become very small and manifests as both a frequency shift of the phonon modes and an asymmetrical broadening of the phonon peaks (58). An examination of the Raman spectra for the hematite films presented in Figure 1 shows that the 250 nm thick film exhibits both blue-shifted frequencies and broader fwhm for all seven phonon peaks compared to the 50 nm thick film. This was quantified by fitting both spectra with seven Lorentzian peaks and comparing results, shown in the Supporting Information. Figure 2 presents just the A_{1g} peak at 229 cm^{-1} where the peak blue shifting and fwhm broadening is clearly observed. This is consistent with results for titanium dioxide powders and films where a blue shift of the frequency and a broadening of the fwhm for the phonon peaks represents decreasing crystallite size (58−62).

The intensity of the Raman scattering increases as the hematite film increases from 50 to 250 nm in thickness. This is intuitive as Raman scattering intensity is proportional to the number density of the interacting media. However, the increase in the signal intensity shown in Figure 1 between the two films is not proportional to the degree of increase in the film thickness. We are unable to explain this; however, as discussed below, IR data do scale appropriately for the hematite films.

Assignments of the six IR active modes of hematite with their respective LO and transverse optical (TO) phonon frequencies are supplied in Table 3. The FTIR spectra collected in transmission mode for the two hematite films are

Table 3. Infrared Active TO and LO Phonon Modes for Hematite from (43, 44) and the Observed Frequencies in This Study

mode assignment	$\omega_{(TO)}$ (cm^{-1})	$\omega_{(LO)}$ (cm^{-1})	This study (cm^{-1})
A_{2u}	299	414	385
A_{2u}	526	662	526
E_u	227	230	N/A
E_u	286	368	N/A
E_u	437	494	436−459
E_u	524	662	526

presented in Figure 3, along with the Lorentzian fits used to quantify the low frequency peak. Spectrum A corresponds to the 50 nm hematite film and spectrum B corresponds to the 250 nm hematite film. The relative absorption intensity between the two spectra shown in Figure 2 is appropriately ∼5 times more intense for spectrum B, as the film is ∼5 times thicker. These spectra feature two prominent peaks at 440 and 526 cm^{-1}. These peaks are assigned to the E_u and A_{2u} + E_u phonon modes, respectively (43, 44). The weak peak present at ∼385 cm^{-1} is attributed to the second A_{2u} mode and is not discussed further (43, 44).

Although both the E_u and the A_{2u} + E_u peaks have been used to characterize hematite thin films and particles, Chernyshova et al. (50) have shown the E_u mode at 440 cm^{-1} to be of greater diagnostic value than the combined A_{2u} + E_u mode at 526 cm^{-1}, as it arises from only one phonon mode. This interpretation is adopted for this study. When considering IR spectroscopy of iron oxides, which exhibit high oscillator strengths, it is necessary to consider the contribution to the spectra from surface modes (50, 69). Surface modes in solids arise when the incoming radiation wavelength is longer than the size of the interacting solid, which is the case for all the thin films investigated here. Because of these induced surface modes, the frequency of the phonon modes within the solid can vary between their TO and LO limits. This effect can be observed as a splitting in the phonon mode peak with contributions from both a

TO and a LO component. A greater contribution from the LO component in the peak frequency has been attributed to an increase in the crystallinity of the hematite sample (50, 69, 70).

Following this interpretation, the spectra presented in Figure 3 show the E_u mode at 440 cm^{-1} fit with two Lorentzian components, one at ∼437 cm^{-1} and one at ∼460 cm^{-1}. An increase in the high frequency component at 460 cm^{-1}, relative to the component at 437 cm^{-1}, has been shown to be correlated with an increase in the degree of crystallinity (50). The two spectra shown in Figure 2 have relative heights of the low frequency component of the E_u mode of 1.60 and 2.13 for A and B, respectively. This indicates that the 50 nm thick hematite film exhibits a higher overall degree of crystallinity than that of the 250 nm thick sample. As the thickness of the hematite film increases from 50 to 250 nm the fwhm for the component peaks of the E_u mode also broadens as indicated in Figure 3 insets. These two findings indicate that the 50 nm hematite film possesses a greater degree of overall crystallinity than the 250 nm thick film, which was also shown by the Raman spectra of these two films.

It is not immediately clear why the 50 nm thick hematite film would possess larger crystal domains than the 250 nm thick film. Using conventional vibrational spectroscopic techniques such as Raman microspectroscopy and FTIR does not allow for an absolute determination of the crystallite size. More traditional methods of size determination such as transmission electron microscopy (TEM) and XRD are also not optimal choices for these samples given that the films are deposited upon a thick, 3 mm, substrate and the films are very thin, respectively. However, by first comparing our results to Chernyshova et al. (50), where both vibrational spectroscopy and TEM/XRD was used to analyze hematite powders of different sizes, it is possible to make an approximation of the size of the crystallites within the thin films presented here. Chernyshova et al. (50) report a relative height intensity of 2.1 for the two components of the E_u mode centered at ∼440 cm^{-1} for 18 nm hematite powder observed in their FTIR spectra. This is very similar to the value of 2.13 for the relative height of the E_u peak components derived for the 250 nm thick hematite film produced in this study. On this basis, a lower bound of approximately 18 nm is proposed for the crystallite domain size within the hematite films produced in this study. The next largest hematite particle size reported by Chernyshova et al. (50) was 39 nm in diameter and had a relative height of the E_u component peaks in the FTIR spectra of 1.4. The 50 nm hematite film from this study has a relative height of the E_u component peaks of 1.6. This indicates that the crystal domains within the 50 nm film are not 39 nm in diameter; however, as it is not possible to quantify the exact size of the domains, 39 nm is proposed as an upper bound on the crystal domain size possessed by the hematite films produced in this study. Phonon confinement has also been used to quantify particle size with frequency shifts and broadening of the phonon peaks within Raman spectra of titanium
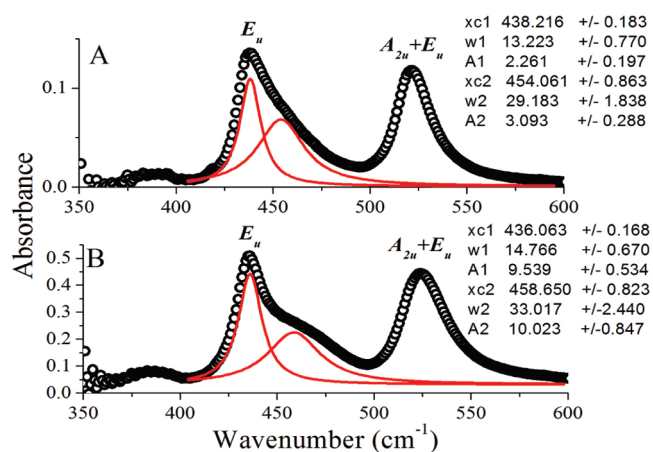

xc1	438.216	+/- 0.183
w1	13.223	+/- 0.770
A1	2.261	+/- 0.197
xc2	454.061	+/- 0.863
w2	29.183	+/- 1.838
A2	3.093	+/- 0.288

xc1	436.063	+/- 0.168
w1	14.766	+/- 0.670
A1	9.539	+/- 0.534
xc2	458.650	+/- 0.823
w2	33.017	+/-2.440
A2	10.023	+/-0.847

FIGURE 3. FTIR spectra of the two hematite samples with the associated fitting of the E_u mode centered at 440 cm^{-1}. Black markers are experiment, red lines are the Lorentzian fitted components. (A) 50 nm film, (B) 250 nm film. Also shown are the results of the Lorentzian fitting procedure (symbols further explained in the Supporting Information).

dioxide powders (58, 60−62). At crystallite sizes above ∼10 nm, the frequency shifts observed become minor, less than 1 cm⁻¹, and phonon confinement becomes a less useful tool for discerning between crystallite size. Here we observe, on average, a frequency shift of approximately 0.5 cm⁻¹ for the hematite phonon modes, Supporting Information, between the 50 and 250 nm thick films. This is not sufficient to quantify the degree of crystallite size change between the two films, but is still useful as it indicates that the 50 nm film does indeed possess a greater degree of crystallinity.

The homogeneity of the films was assessed by running a spectral mapping experiment, where a Raman spectrum was collected at every 100 um point across a large section of the film, ∼1.5 mm in length (see the Supporting Information). There were no significant detectable differences in peak frequency or fwhm for the spectra collected in this way for either film. This indicates that, within the limit of detection, the phase is homogeneous across the film. While there are differences in scattering intensity between different spots for the 250 nm film, this is presumed to arise from differing surface roughness of the film in different spots and not from any compositional change in the phase of the oxide.

The Fe films annealed for 4 h at 575 °C are demonstrated to exhibit the Raman and FTIR signatures that are consistent with an assignment of the oxide phase to hematite. The extraneous peak at 660 cm⁻¹ in the Raman spectra is representative of disorder within the crystal lattice and not residual magnetite contamination (15, 50, 54, 68). Both Raman microspectroscopy and FTIR were used to address the crystallinity of the hematite films where the 50 nm film exhibits a greater degree of crystallinity than the 250 nm thick film. Using a comparison with Chernyshova et al. (50) results, a range of 18−39 nm is proposed for the size of the crystallites within the hematite films. By lowering the annealing temperature to 350 °C, it is possible to produce the iron oxide polymorph maghemite, instead of hematite.

Maghemite. Maghemite films were prepared by heating the Fe films at 350 °C for four hours, which was sufficient to oxidize the initial Fe films fully, but still avoid hematite formation as indicated by the Raman spectra containing peaks associated with those phases (data not shown). This temperature selection was important, as heating at 325 °C was insufficient to completely oxidize the film to maghemite and an increase to 375 °C resulted in hematite contamination. Hence, deviation from 350 °C annealing temperature resulted in significant magnetite or hematite formation in the films.

If the vacancies in the maghemite structure are randomly distributed then the net structure will exhibit spinel symmetry (8−10). The expected vibrational modes of the first Brillouin zone center of a spinel structure are given by eq 3 (49, 71)

$$\Gamma_{vib} = A_{1g} + E_{1g} + T_{1g} + 3T_{2g} + 2A_{2u} + 2E_u + 4T_{1u} + 2T_{2u} \quad (3)$$
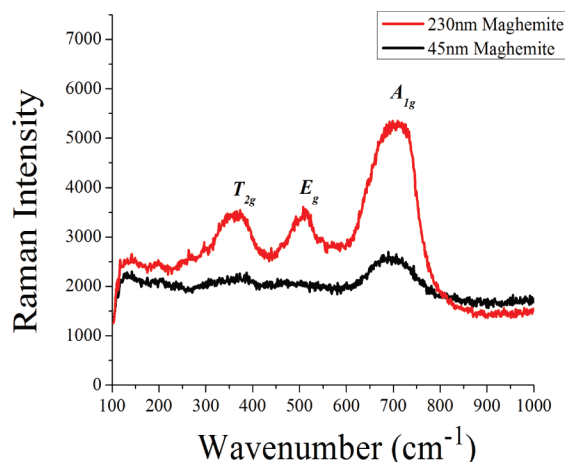

FIGURE 4. Raman spectra of maghemite films with the phonon peak assignments. No peaks corresponding to hematite contamination are present.

All modes are observable except the T_{1g}, A_{2u}, E_u, and T_{2u} modes, which are optically silent. The remaining symmetrical modes ($A_{1g} + E_g + 3T_{2g}$) are Raman active, and the $4T_{1u}$ modes are infrared active (10, 49, 71).

The Raman spectra of the two maghemite films are presented in Figure 4. The frequency of maghemite's Raman active phonon modes is known to vary with preparation method and the distribution of vacancies within the maghemite crystal unit cell (47). However, the spectra presented in Figure 4 match Raman spectra for maghemite previously reported in literature (47, 48, 50, 54, 70). Maghemite has three observed Raman active phonon modes at 365 cm⁻¹ (T_{2g}), 511 cm⁻¹ (E_g), and 700 cm⁻¹ (A_{1g}), Table 2, that exhibit a broad scattering response (10, 47). The weak Raman signal for the maghemite films in Figure 4 is due to maghemite's poor scattering response (47). For the 45 nm film, Figure 4, weak phonon modes at 365 and 511 cm⁻¹ give a very slight scattering response. As the thickness of the maghemite film increases from 45 to 230 nm, Figure 4, the T_{2g} and E_g phonon modes at 365 and 511 cm⁻¹ become much more pronounced. This weak response is likely due to poor scattering properties of maghemite; zooming in on the spectra presented in Figure 4 though shows that the relative height ratio between the A_{1g} peak and the T_{2g} peak is roughly the same value, $A_{1g}/T_{2g} \approx 2$, for both the 230 nm and the 45 nm films. The roughness of the fits for the maghemite films used here should be stressed as the broadness of the maghemite Raman response makes fitting difficult. The Lorentzian parameters used to fit the data are presented in the Supporting Information. Attempts to increase signal-to-noise in the maghemite Raman spectra by increasing the acquisition time resulted in irreversible hematite formation. For the 45 nm thick maghemite film only the A_{1g} peak at 700 cm⁻¹ is pronounced. This is sufficient to assign this film to the maghemite phase as this feature has been shown to only be associated with maghemite formation (10, 47, 54, 57). No features associated with laser induced phase changes can be seen for the maghemite films in Figure 4. The homogeneity of the films was checked in a similar manner to that of the hematite films and was found to yield spectra indicative
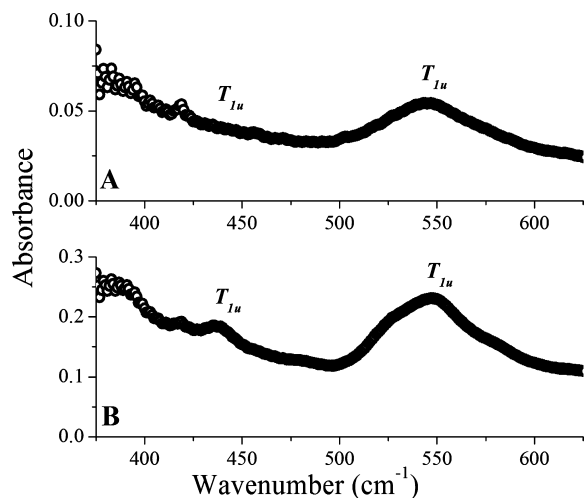
FIGURE 5. FTIR spectra of maghemite films. (A) 45 nm film, (B) 230 nm film. Prominent T_{1u} mode visible at 550 cm^{-1} for both films.

of maghemite phase across the films (see the Supporting Information).

Phonon confinement effects can also be observed for the maghemite films. Similarly to hematite, the thinner films exhibit both a red-shifted peak frequency and a narrower fwhm for the main A_{1g} peak, indicating a greater degree of crystallinity. Because of the very broad Raman scattering response for maghemite and the frequency shifts that can occur with different preparation techniques, it appears that phonon confinement is a less useful tool for the investigation of maghemite crystallinity than materials with sharp, strong Raman peaks.

Shown in Figure 5 are the FTIR spectra for the two maghemite films. If the maghemite samples possess spinel crystal structure, then there are four T_{1u} phonon modes expected at 212, 362, 440, and 553 cm^{-1} (10), of which we are able to observe the highest two frequency modes with our existing experimental setup. The 230 nm thick film exhibits clearly the two T_{1u} modes expected around 440 and 550 cm^{-1} for maghemite, whereas the thinner, 45 nm, film exhibits a peak at 546 cm^{-1} (10). The lack of the T_{1u} peak at 440 cm^{-1} for the thinner film is attributed to weak absorption due to the very thin nature of the film. The thicker film exhibits roughly 5× the absorbance of the thinner film for the T_{1u} mode at ~550 cm^{-1}, as is expected.

The appearance of the peaks attributed to the two T_{1u} modes confirms that the vacancies in the maghemite crystal structure are randomly distributed resulting in a spinel crystal structure. If this was not the case, many more strongly absorbing vibrational phonon modes would be expected (8, 9). Additionally, the thicker film shows some spectral structure at ~430 and ~525 cm^{-1}. These features may be indicative of slight hematite contamination; however, there are no hematite features observed in the Raman spectra presented in Figure 4 for the maghemite films. These FTIR spectral features may also potentially arise from minor deviation in the ordering of the vacancies which has been shown to produce additional modes (8, 9). Yet, the assignment of these low-intensity peaks remains ambiguous. The TO/LO phonon splitting has been calculated for the observed

Table 4. TO/LO Splitting for the Observed Maghemite IR Phonon Modes Calculated from Glotch et al. (8) Optical Constants, and Observed Frequencies for These Modes from Maghemite Films Prepared in This Study

mode assignment	$\omega_{(TO)}$ (cm^{-1})	$\omega_{(LO)}$ (cm^{-1})	observed (cm^{-1})
$T_{1u}(1)$	440	453	439 (230 nm film)
$T_{1u}(2)$	550	572	546 (45 nm film)
			547 (230 nm film)

phonon modes from the optical constants for maghemite from Glotch et al. (8), Table 4, and is ~13 cm^{-1} for the T_{1u} mode centered around 440 and ~22 cm^{-1} for the mode centered at 550 cm^{-1}. The observed FTIR phonon frequencies for the maghemite films lie slightly below the TO frequency limit; however, frequency of maghemite phonon modes is known to depend heavily upon preparation method and this is attributed as the source of the observed red shift (8, 9). The low degree of phonon splitting is expected for solids possessing spinel structure (72) and prevents an analysis of the net crystallinity of the films via FTIR as was done for hematite. However, the broadening and blue shifting of the A_{1g} mode in Figure 4 as the film thickness increases does indicate that the 45 nm thick maghemite film possesses a greater degree of crystallinity than the 230 nm thick film.

Heating the Fe films at 350 °C for 4 h produced maghemite films, which were then characterized by Raman microspectroscopy and FTIR. The phase of the oxide films were confirmed by Raman and FTIR spectra, which are indicative of maghemite formation. The FTIR spectra contain two main peaks assigned to the T_{1u} modes of the spinel structure. This indicates that the vacancies within the crystal structure are randomly distributed. As the films increase in thickness, the signature Raman peaks both broaden and blue shift, suggesting that the thinner film possesses a greater degree of crystallinity. To produce the least oxidized phase reported here, magnetite, a much lower annealing temperature of 175 °C was chosen.

Magnetite. Magnetite possesses spinel symmetry similar to maghemite. Hence, the normal modes of vibration for the first Brillouin zone center are expected to be given by eq 3 as well. The magnetite films are thinner than both the hematite and maghemite films because of magnetite's inverse spinel crystal structure that possesses a smaller unit cell than hematite and is free of vacancies unlike maghemite. The Raman spectra of the two magnetite films produced are shown in Figure 6. Choice of laser power and acquisition time is vital for collecting magnetite Raman spectra as phase changes are easily induced in the films by the excitation laser. At acquisition times longer than 30 s at 6 mW (100 %) laser power hematite features were observed in collected spectra (not shown). The spectra in Figure 6 agree well with reported spectra in the literature without any features indicating either maghemite or hematite contamination (10, 47−49, 57). The pronounced magnetite feature at 670 cm^{-1}, attributed to the A_{1g} mode, is visible in both spectra of Figure 6 (49). The features at 300 and 550 cm^{-1} are weak
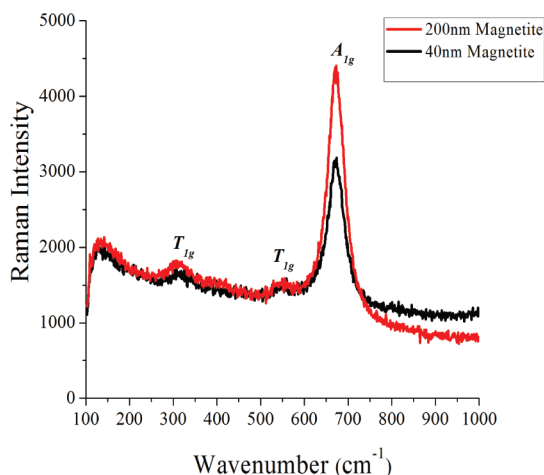
FIGURE 6. Raman spectra of magnetite films. Only A_{1g} mode at 670 cm^{-1} is pronounced.
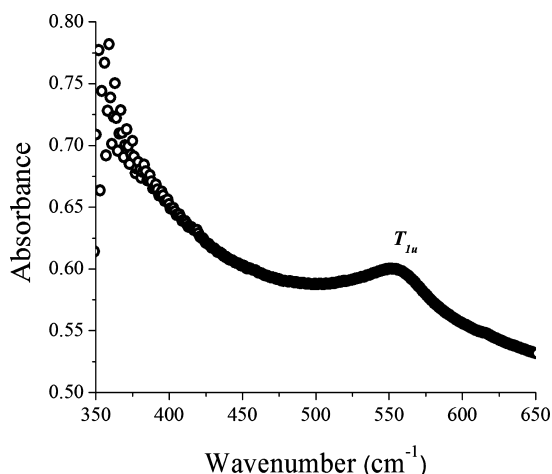

FIGURE 7. FTIR spectrum of 40 nm thick magnetite film. Only T_{1u} mode at 560 cm^{-1} is observed. Recorded intensity is not meaningful because of reflection losses from the oxide film.

in both spectra and are assigned to the T_{1g} vibrational mode (49). There is no observable peak shifting in the Raman spectra with an increase in the film thickness from 40 to 200 nm; however, the T_{1g} mode at 670 cm^{-1} does broaden as the thickness increases. This broadening indicates that the thinner magnetite film possess greater crystallinity than the thicker film, as is also the result for the hematite and maghemite films. A Raman mapping experiment was conducted indicating that the films are homogeneous across a large section of the film (see the Supporting Information).

FTIR spectra were collected for the magnetite films. However, because of the reflective nature of the films, little transmission intensity was recorded, even for the 40 nm film. It is possible to observe a T_{1u} mode at 560 cm^{-1} for the 40 nm film as shown in Figure 7, but the absorbance intensity of the mode is not meaningful because of reflection losses from the film. The frequency of this mode agrees well with reported values by literature (10, 49, 71). The other commonly observed T_{1u} magnetite mode at 350 cm^{-1} is cut off because of absorption by the KBr substrate. Magnetite, like maghemite, exhibits a low degree of TO/LO phonon mode splitting. Using the optical constants for magnetite presented by Glotch et al. (8), the phonon mode splitting for

Table 5. Calculated TO/LO Phonon Splitting from Optical Constants from Glotch et al. (8) and the Observed Frequency for the T_{1u} Mode

mode assignment	$\omega_{(TO)}$ (cm^{-1})	$\omega_{(LO)}$ (cm^{-1})	observed (cm^{-1})
T_{1u}	558	576	560 (40 nm film)

the T_{1u} mode of magnetite at 560 cm^{-1} was calculated in this study to be ~19 cm^{-1}, Table 5. This is in excellent agreement with the phonon splitting calculated for various other spinel materials (72). The low degree of phonon splitting for magnetite as well as the inability to produce a useable spectrum for the 200 nm thick film makes it difficult to use the FTIR spectrum presented in Figure 7 to discuss the degree of crystallinity exhibited by the thin magnetite films.

CONCLUSIONS

In this study, the preparation of thin films (40−250 nm) of three common iron oxide polymorphs: hematite, maghemite, and magnetite, using a conventional electron beam evaporation technique is presented. The advantage of producing the oxide films using electron beam evaporation is the absence of any unwanted precursor chemicals. These films were then characterized with the vibrational spectroscopic methods of Raman microspectroscopy and FTIR, allowing for clear phase assignment of the thin oxide film produced. As well as phase assignment, crystallinity of the samples was examined using the phonon confinement phenomena from the Raman results and the degree of splitting of the TO/LO components of the phonon modes present in the FTIR spectra. For films of all three iron oxide polymorphs produced, the thinner films exhibit a greater degree of crystallinity than the thicker films. The explanation of this remains ambiguous. However, this study represents the first time to the authors' knowledge that Raman microspectroscopy and FTIR have been used in conjuncture to investigate the relative degree of crystallinity possessed by synthetic iron oxide thin films.

APPENDIX A

The iron oxide film thickness was estimated by calculating the approximate number of Fe atoms present in the film

$$D\left(\frac{g}{cm^3}\right)A_{substrate}(cm^2)d(cm)\frac{1}{amu\ of\ Fe}\left(\frac{mol}{g}\right)(6.02\times10^{23})$$

$$\left(\frac{atoms}{mol}\right) = \text{no. of Fe atoms} \quad \text{(A.1)}$$

where D is the density of iron, A is the area of the substrate, and d is the thickness of the initial deposited Fe film. This allows the calculation of the number of oxide unit cells present as the number of iron atoms per unit cell is known

$$\frac{\text{total no. of Fe atoms}}{\text{no. of Fe atoms per unit cell}} = \text{no. of oxide unit cells} \tag{A.2}$$

By examining the cross-sectional area of a sample unit cell and the total area of the substrate the number of unit cells needed to form one layer on the substrate is calculated

$$\frac{A_{\text{substrate}}}{A_{\text{unit cell}}} = \text{no. of unit cells to form one layer} \tag{A.3}$$

With the total number of unit cells present in the film and the number of unit cells needed to form a layer the total oxide film thickness is calculated as

$$\frac{\text{no. of unit cells}_{\text{total}}}{\text{no. of unit cells}_{\text{first layer}}} C \ (\text{m}) =$$

$$\text{iron oxide film thickness (m)} \tag{A.4}$$

Here, C is the third axis of the unit cell not picked to calculate the cross-sectional area of the unit cell. Results from this estimate agree well with our measured ellipsometry thicknesses.

Note Added after ASAP Publication. This paper was published on the Web on Sep 8, 2010, with errors in Equation 2. The corrected version was reposted on Sep 13, 2010.

Supporting Information Available: Raman spectra from $100-2000 \ \text{cm}^{-1}$ for hematite, maghemite, and magnetite films; Lorentzian fits and fitting parameters to Raman spectra for hematite and maghemite films; Raman spectral mapping results for hematite, maghemite, and magnetite films; and optical microscopy images with $50\times$ objective for hematite, maghemite, and magnetite films (PDF). This material is available free of charge via the Internet at http://pubs.acs.org.

REFERENCES AND NOTES

(1) Cornell, R. M.; Schwertmann, U. *The Iron Oxides: Structure, Properties, Reactions, Occurrences and Uses*, 2nd ed.; Wiley-VCH: Wienheim, Germany, 2003.

(2) Eggleston, C. M.; Hug, S.; Stumm, W.; Sulzberger, B.; Afonso, M. D. S. *Geochim. Cosmochim. Acta* **1998**, *62* (4), 585–593.

(3) Hug, S. J. *J. Colloid Interface Sci.* **1997**, *188*, 415–422.

(4) Lefevre, G. *Adv. Colloid Interface Sci.* **2004**, *107*, 109–123.

(5) Lefevre, G.; Fedoroff, M. *Phys. Chem. Earth* **2006**, *31*, 499–504.

(6) Arai, Y.; Sparks, D. L.; Davis, J. A. *Environ. Sci. Technol.* **2004**, *38*, 817–824.

(7) Fukushi, K.; Sverjensky, D. A. *Geochim. Cosmochim. Acta* **2007**, *71*, 1–24.

(8) Glotch, T. D.; Rossman, G. R. *Icarus* **2009**, *204*, 663–671.

(9) Pecharroman, C.; Gonzales-Carreno, T.; Iglesias, J. E. *Phys. Chem. Miner.* **1995**, *22*, 21–29.

(10) Chamritski, I.; Burns, G. *J. Phys. Chem. B* **2005**, *109*, 4965–4968.

(11) Fleet, M. E. *Acta Crystallogr., Sect. B* **1981**, *37* (4), 917–920.

(12) Poghossian, A. S.; Abovian, H. V.; Aroutiounian, V. M. *Sens. Actuators, B* **1994**, *18−19*, 155–157.

(13) Viefhaus, H.; Hennesen, K.; Lucas, M.; Muller-Lorenz, E. M.; Grabke, H. J. *Surf. Interface Anal.* **1994**, *21*, 665–672.

(14) Lottici, P.; Baratto, C.; Bersani, D.; Antonioli, G.; Montenero, A.; Guarneri, M. *Opt. Mater.* **1998**, *9*, 368–372.

(15) Bersani, D.; Lottici, P. P.; Montenero, A. *J. Raman Spectrosc.* **1999**, *30*, 355–360.

(16) Yubero, F.; Ocana, M.; Justo, A.; Contreras, L.; Gonzalez-Elipe, A. R. *J. Vac. Sci. Technol., A* **2000**, *18* (5), 2244–2248.

(17) Miller, E. L.; Paluselli, D.; Marsen, B.; Rocheleau, R. E. *Thin Solid Films* **2004**, *466*, 307–313.

(18) Peulon, S.; Antony, H.; Legrand, L.; Chausse, A. *Electrochim. Acta* **2004**, *49*, 2891–2899.

(19) Desai, J. D.; Pathan, H. M.; Min, S.; Jung, K.; Joo, O. S. *Appl. Surf. Sci.* **2005**, *252*, 1870–1875.

(20) Martinez, L.; Leinen, D.; Martin, F.; Gabas, M.; Ramon-Barrado, J. R.; Quagliata, E.; Dalchiele, E. A. *J. Electrochem. Soc.* **2007**, *154* (3), D126–D133.

(21) Wei, Q.; Zhang, Z.; Li, Z.; Zhou, Q.; Zhu, Y. *J. Phys. D: Appl. Phys.* **2008**, *41*, 202002 (4pp).

(22) Fu, D.; Wren, J. C. *J. Nucl. Mater.* **2008**, *374*, 116–122.

(23) Aronniemi, M.; Saino, J.; Lahtinen, J. *Thin Solid Films* **2008**, *516*, 6110–6115.

(24) Wang, W.; Liang, L.; Johs, A.; Gu, B. *J. Mater. Chem.* **2008**, *18*, 5770–5775.

(25) Park, Y. J.; Sobahan, K. M. A.; Hwangbo, C. K. *Surf. Coat. Technol.* **2009**, *203*, 2646–2650.

(26) Vurens, G. H.; Salmeron, M.; Somorjai, G. A. *Surf. Sci.* **1988**, *201*, 129–144.

(27) Weiss, W.; Barbieri, A.; Van Hove, M. A.; Somorjai, G. A. *Phys. Rev. Lett.* **1993**, *71* (12), 1848–1851.

(28) Barbieri, A.; Weiss, W.; Van Hove, M. A.; Somorjai, G. A. *Surf. Sci.* **1994**, *302*, 259–279.

(29) Schedel-Niedrig, Th.; Weiss, W.; Schlogl, R. *Phys. Rev. B: Condens. Matter Mater. Phys.* **1995**, *52* (24), 17449–17460.

(30) Peng, Y.; Park, C.; Laughlin, D. E. *J. Appl. Phys.* **2003**, *93* (10), 7957–7959.

(31) Weiss, W.; Sormorjai, G. A. *J. Vac. Sci. Technol., A* **1993**, *11* (4), 2138–2144.

(32) Ritter, M.; Over, H.; Weiss, W. *Surf. Sci.* **1997**, *371*, 245–254.

(33) Ritter, M.; Ranke, W.; Weiss, W. *Phys. Rev. B: Condens. Matter Mater. Phys.* **1998**, *57* (12), 7240–7251.

(34) Ritter, M.; Weiss, W. *Surf. Sci.* **1999**, *432*, 81–94.

(35) Weiss, W.; Ritter, M. *Phys. Rev. B: Condens. Matter Mater. Phys.* **1999**, *59* (7), 5201–5213.

(36) Joseph, Y.; Ranke, W.; Weiss, W. *J. Phys. Chem. B* **2000**, *104*, 3224–3236.

(37) Ketteler, G.; Weiss, W.; Ranke, W. *Surf. Rev. Lett.* **2001**, *8* (6), 661–683.

(38) Kim, Y. J.; Gao, Y.; Chambers, S. A. *Surf. Sci.* **1997**, *371*, 358–370.

(39) Kim, Y. J.; Westphal, C.; Ynzunza, R. X.; Wang, Z.; Galloway, H. C.; Salmeron, M.; Van Hove, M. A.; Fadley, C. S. *Surf. Sci.* **1998**, *416*, 68–111.

(40) Barbieri, A.; Belkhou, R.; Ohresser, P.; Gautier-Soyer, M.; Besencent, O.; Mulazzi, M.; Guittet, M. J.; Moussy, J. B. *Phys. Rev. B: Condens. Matter Mater. Phys.* **2005**, *72* (1−7), 245423.

(41) Lazzari, J. P.; Melnick, I.; Randet, D. *IEEE Trans. Magn.* **1967**, *MAG3* (3), 205-&.

(42) McCarty, K. F. *Solid State Commun.* **1988**, *68* (8), 799–802.

(43) Onari, S.; Arai, T.; Kudo, K. *Phys. Rev. B: Condens. Matter Mater. Phys.* **1977**, *16* (4), 1717–1721.

(44) Serna, C. J.; Rendon, J. L.; Iglesias, J. E. *Spectrochim. Acta, Part A* **1982**, *38A* (7), 797–802.

(45) Nasrazadani, S.; Raman, A. *Corros. Sci.* **1993**, *34* (8), 1355–1365.

(46) Bell, J. F., III; Roush, T. L.; Morris, R. V. *J. Geophys. Res.* **1995**, *100* (E3), 5297–5307.

(47) de Faria, D. L. A.; Silva, S. V.; de Oliveira, M. T. *J. Raman Spectrosc.* **1997**, *28*, 873–878.

(48) Oh, S. J.; Cook, D. C.; Townsend, H. E. *Hyperfine Interact.* **1998**, *112* (1−4), 59–65.

(49) Gasparov, L. V.; Tanner, D. B.; Romero, D. B.; Berger, H.; Margaritondo, G.; Forro, L. *Phys. Rev. B: Condens. Matter Mater. Phys.* **2000**, *62* (12), 7939–7944.

(50) Chernyshova, I. V., Jr.; Madden, A. S. *Phys. Chem. Chem. Phys.* **2007**, *9*, 1736–1750.

(51) van der Weerd, J.; Rehren, T.; Firth, S.; Clark, R. J. H. *Mater. Charact.* **2004**, *53*, 63–70.

(52) Nie, X.; Li, X.; Du, C.; Huang, Y.; Du, H. *J. Raman Spectrosc.* **2008**, *40*, 76–79.

(53) Shebanova, O. N.; Lazor, P. *J. Solid State Chem.* **2003**, *174*, 424–430.

(54) Modesto Lopez, L. B.; Pasteris, J. D.; Biswas, P. *Appl. Spectrosc.* **2009**, *63* (6), 627–635.

(55) Massey, M. J.; Baier, U.; Merlin, R.; Weber, W. H. *Phys. Rev. B: Condens. Matter Mater. Phys.* **1990**, *41* (11), 7822–7827.

(56) Campbell, I. H.; Fauchet, P. M. *Solid State Commun.* **1986**, *58* (10), 739–741.

(57) Hanesch, M. *Geophys. J. Int.* **2009**, *177*, 941–948.

(58) Bersani, D.; Lottici, P. P.; Ding, X. Z. *Appl. Phys. Lett.* **1998**, *72* (1), 73–75.

(59) Demopoulos, G. P.; Charbonneau, C.; Lee, K. E.; Shan, G. B.; Gomez, M. A.; Gauvin, R. *ECS Trans.* **2009**, *21* (1), 23–34.

(60) Gupta, S. K.; Desai, R.; Jha, P. K.; Sahoo, S.; Kirin, D. *J. Raman Spectrosc.* **2009**, *41*, 350–355.

(61) Balaji, S.; Djaoued, Y.; Robichaud, J. *J. Raman Spectrosc.* **2006**, *37*, 1416–1422.

(62) Zhang, W. F.; He, Y. L.; Zhang, M. S.; Yin, Z.; Chen, Q. *J. Phys. D: Appl. Phys.* **2000**, *33*, 912–916.

(63) Batur, C.; Vhora, M. H.; Cakmak, M.; Serhatkulu, T. *ISA Trans.* **1999**, *38*, 139–148.

(64) Owens, F. J.; Orosz, J. *Solid State Commun.* **2006**, *138*, 95–98.

(65) Richter, H.; Wang, Z. P.; Ley, L. *Solid State Commun.* **1981**, *39*, 625–629.

(66) DeBoer, F. E.; Selwood, P. W. *J. Am. Chem. Soc.* **1954**, *76* (13), 3365–3367.

(67) Porto, S. P. S.; Krishnan, R. S. *J. Chem. Phys.* **1967**, *47* (3), 1009–1012.

(68) Xu, Y. Y.; Zhao, D.; Zhang, X. J.; Jin, W. T.; Kashkarov, P.; Zhang, H. *Phys.E* **2009**, *41*, 806–811.

(69) Tolstoy, V. P.; Chernyshova, I. V.; Skryshevsky, V. A. *Handbook of Infrared Spectroscopy of Ultrathin Films*.; Wiley-VCH: Weinheim, Germany, 2003.

(70) Serna, C. J.; Iglesias, J. E. *J. Mater. Sci. Lett.* **1986**, *5* (9), 901–902.

(71) White, W. B.; DeAngelis, B. A. *Spectrochim. Acta, Part A* **1967**, *23A*, 985–995.

(72) Shirai, H.; Morioka, Y.; Nakagawa, I. *J. Phys. Soc. Jpn.* **1982**, *51* (2), 592–597.